Batteries & Supercaps

Research Article
doi.org/10.1002/batt.202300167

Chemistry Europe
European Chemical Societies Publishing

www.batteries-supercaps.org

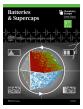

Optimizing the Composite Cathode Microstructure in All-Solid-State Batteries by Structure-Resolved Simulations

Moritz Clausnitzer,*[a, b] Robert Mücke,[c] Fadi Al-Jaljouli,[c, d] Simon Hein,[a, b] Martin Finsterbusch,[c] Timo Danner,[a, b] Dina Fattakhova-Rohlfing,[c] Olivier Guillon,[c, d] and Arnulf Latz[a, b, e]

All-solid-state batteries are considered as an enabler for applications requiring high energy and power density. However, they still fall short of their theoretical potential due to various limitations. One issue is poor charge transport kinetics resulting from both material inherit limitations and non-optimized design. Therefore, a better understanding of the relevant properties of the cathode microstructure is necessary to improve cell performance. In this article, we identify optimization potentials of the composite cathode by structure-resolved electrochemical 3D-simulations. In our simulation study, we investigate the influence of cathode active material fraction, density, particle size, and active material properties on cell performance. Special focus is set on the impact of grain boundaries on the cathode design. Based on our simulation results, we can predict target values for cell manufacturing and reveal promising optimization strategies for an improved cathode design.

Introduction

Batteries play a crucial role in the transition to renewable energy systems, particularly in the electrification of transportation and the growing sector coupling.[1] Li-ion batteries are the primary choice for electric vehicles as they offer a cost-effective energy storage solution with high energy and power density.[2] In recent years, large-scale production of lithium-ion batteries has significantly increased and prices are approaching 150 $/kWh.[3] Despite these advances, conventional Li-ion batteries are reaching their technological limits.[4] This leads to the development of new battery types among which all-solid-state batteries (ASSBs) are considered especially interesting for automotive applications. ASSBs use solid electrolytes (SEs), which have the potential to enable the use of Li metal at the negative electrode, resulting in a significant increase in energy density.[5–7] Additionally, the unique properties of SEs can improve battery safety and rate capability.[8] Four main classes of SEs are generally distinguished: polymers, sulfides, oxides and halides.[9–11] Among the different types of SEs, the ceramic garnet-type electrolyte $Li_7La_3Zr_2O_{12}$ (LLZO) stands out due to its wide electrochemical stability window, reasonable ionic conductivity, and good thermal stability.[12] However, the manufacturing of dense pellets typically includes a high-temperature sintering step, which increases production costs and can cause detrimental side reactions and secondary phases in contact with the cathode active material (CAM).[13–17] Moreover, the effect of grain boundaries is most prominent in LLZO and can reduce the Li-ion conductivity significantly.[18]

A key component of an ASSB is the composite cathode, that determines both the achievable energy and power density. To improve storage capacity and energy density, the amount of CAM in the battery must be maximized. At the same time, to achieve practical current and power densities, the cathode design should offer a large surface area and short transport pathways.[17] These requirements are typically met in a 3D network of SE and CAM particles. Ideally, both materials form a percolating network that enables efficient charge transport of both ions in the SE phase and electrons in the CAM phase. In a

[a] M. Clausnitzer, Dr. S. Hein, Dr. T. Danner, Prof. Dr. A. Latz
German Aerospace Center (DLR)
Institute of Engineering Thermodynamics
Pfaffenwaldring 38–40
70569 Stuttgart, Germany
E-mail: moritz.clausnitzer@dlr.de

[b] M. Clausnitzer, Dr. S. Hein, Dr. T. Danner, Prof. Dr. A. Latz
Helmholtz Institute Ulm for Electrochemical Energy Storage (HIU)
Helmholtzstraße 11
89081 Ulm, Germany

[c] Dr. R. Mücke, F. Al-Jaljouli, Dr. M. Finsterbusch, Prof. Dr. D. Fattakhova-Rohlfing, Prof. Dr. O. Guillon
Forschungszentrum Jülich GmbH
Institute of Energy and Climate Research
Materials Synthesis and Processing (IEK-1)
Wilhelm-Johnen-Straße
52425 Jülich, Germany
and
Jülich Aachen Research Alliance: JARA-Energy
52425 Jülich, Germany

[d] F. Al-Jaljouli, Prof. Dr. O. Guillon
RWTH Aachen University
Institute of Mineral Engineering
Department of Ceramics and Refractory Materials
52064 Aachen, Germany

[e] Prof. Dr. A. Latz
Ulm University, Institute of Electrochemistry
Albert-Einstein-Allee 47
89081 Ulm, Germany

Supporting information for this article is available on the WWW under https://doi.org/10.1002/batt.202300167

conventional Li-ion battery, liquid electrolyte infiltrates the porous CAM structure, naturally forming the required 3D network. However, in case of an ASSB, SE and CAM particles must be mixed and densified. Any significant remaining pores in the structure negatively impact battery performance by blocking transport pathways and reducing the surface area for charge transfer. Besides, composite cathodes in ASSBs feature a high number of solid-solid interfaces that pose an additional barrier for charge transfer.[19] Structure formation and cell performance are significantly influenced by the electrode composition and particle sizes of both SE and CAM. Therefore, the microstructure of the composite cathode and the corresponding processing require careful optimization.[17,20,21] In addition, the cathode is prone to electrochemical and mechanical degradation during cell manufacturing and operation. These can lead to the formation of secondary phases and voids, which impede charge transfer and significantly limit cell performance.[17,21]

Recent research has focused on the optimization of the composite cathode. Both experimental and theoretical groups studied various aspects of electrode design.[17,22–37] It has been shown that increasing the CAM fraction causes lower effective ionic conductivity as a result of a higher tortuosity in the electrolyte phase. Similarly, a decreasing CAM fraction leads to lower effective electronic conductivity of the CAM network.[22–28] The choice of SE and CAM particle size is complex, as the optimum SE particle size depends on the size of the contained CAM particles and vice versa. Generally, SE particles should be smaller than CAM particles to ensure good SE/CAM contact.[24,29] Small SE particles contribute to good ionic percolation, homogeneous material distribution, and low tortuosity in the electrolyte phase.[22] However, grain boundaries increase the charge transfer resistance reducing the effective conductivity of the electrolyte.[19,29,38,39] A tailored particle size can help to reduce the residual porosity in the composite cathode and, thus, increase the cell performance.[23,37] With regard to the active material, the particle size influences the formation of a percolation network as well as the mean diffusion length in the CAM.[21,30]

To reduce experimental effort, microstructure-resolved simulations can be an effective tool for optimization of the composite cathode microstructure.[31–36,38] Bielefeld et al. investigated the effect of the structural properties of the composite cathode on the cell performance for the material system $LiNi_{0.8}Co_{0.1}Mn_{0.1}O_2$ (NMC811)/Li_6PS_5Cl.[35,36] GB effects in the SE are generally expected to be minor in Li_6PS_5Cl and were, consequently, neglected in this study.[36] Finsterbusch et al. used a FIB-SEM reconstruction of a $LiCoO_2$ (LCO)/LLZO cathode as basis for structure-resolved simulations. In their study, the cathode structure was altered to investigate the influence of pore space and cathode thickness..[31] The SE was treated as homogeneous phase not resolving individual GBs. In 2021, Neumann et al. introduced a new model to describe the charge transfer resistance at grain boundaries, modeling a trilayer concept for an ASSB with LLZO electrolyte.[38,40,41] This model allows for efficient simulation of grain boundary resistances without spatially resolving them explicitly.

In this study, we present electrochemical structure-resolved simulations of LLZO-based cells with composite cathodes. Our virtual microstructures resemble 3D reconstructions of LCO/LLZO cathodes produced in a sintering step. In our simulations we specifically take into account the effect of grain boundaries in the SE. This approach allows for the first time to consistently consider the effect of different SE and CAM particle size in the optimization of the composite microstructure. In the first part of this article, we present the corresponding structure generation and simulation methods. Next, we identify limiting factors for electrochemical performance considering the CAM fraction (Influence of the CAM fraction), density (Influence of the density after sintering), and particle sizes (Influence of the SE and CAM particle size) of the composite cathode. Finally, we compare the electrochemical performance of the active materials LCO and NMC811 providing an outlook for future cell chemistries. From our simulation results, we derive optimization strategies for an improved composite cathode design. While we focus on the materials LLZO and LCO, it's worth noting that the optimization strategies and protocols can be readily applied to other material systems as well. While the predictions in this article are based on computational studies, they provide valuable insights into potential improvements in the cathode microstructure and offer a better understanding of the factors limiting cell performance.

Simulation Methodology

Simulation workflow

Our electrochemical simulations are based on a number of virtual cathode structures with varying cathode active material fractions, densities, and particle sizes. These structures are generated with a process-mimetic algorithm in the software package GeoDict (Math2Market GmbH, Kaiserslautern, Germany). To account for grain boundaries in the solid electrolyte, the SE phase in the structures is segmented into individual particles using a watershed algorithm. The electrochemical model is then solved on a voxel-based computational grid representing the composite cathode, anode, separator, and current collectors. Our simulations intrinsically consider the structural properties of the electrodes, providing insights into the performance-limiting structural properties and underlying physical processes.[31–33,38] Therefore, we additionally determine geometric parameters of the cathode microstructures, including tortuosity, active area, and connectivity. These values are used to interpret the electrochemical simulation results and correlate them with the geometric properties. Figure 1 provides an overview of the workflow in this study.

Microstructure generation and virtual cell assembly

Structure generation

The microstructures of the composite cathode were generated by material design using the software GeoDict by the following

Research Article
doi.org/10.1002/batt.202300167
Chemistry Europe
European Chemical Societies Publishing

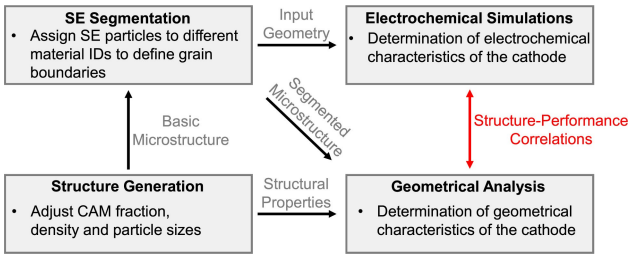

Figure 1. Overview of the workflow to determine the influence of the geometrical properties on the electrochemical cell performance of the composite cathode.

steps.[42] 1) A mixture of grains of CAM and LLZO was piled (sedimented) in the first step. In Table S1, the shapes, volume fractions and sizes of the piled particles are summarized. The target CAM volume fraction was used to scale the total volume fraction and the target volumetric mean diameter to scale the dimensions uniformly. A total domain of 250×250×650 voxels (25 μm×25 μm×65 μm) with a voxel length of 100 nm was filled with particles parallel to the largest (z) axes. 2) In the next step, the domain was cropped to 250×250×500 voxels (25 μm×25 μm×50 μm) while being centered to remove regions of lower packing density and deviating CAM solid volume fractions. 3) In order to prevent unrealistic shading effects from the piling, the particles were distributed for uniform spacing. 4) The structure was sintered to the desired density using the Voronoi tessellation algorithm in GeoDict.[43] 5) The final achieved solid volume fraction of the CAM and the density were checked with the target values and steps 1–4 were repeated with adjusted input values for the solid volume fraction of the CAM and the density if necessary to ensure maximum deviations of 0.25 %. Hereby, the DFSANE algorithm (derivative-free spectral approach for solving nonlinear systems of equations) was employed.[44] An example generation of the microstructure can be found in Figure S1. Note that throughout this manuscript, when referring to particle size, we specifically refer to the mean particle diameter before the geometric sintering process, which can be interpreted as the mean particle size of the powder materials.

SE Segmentation

We segment the electrolyte in the virtual microstructures using a marker-based watershed algorithm[45] to resolve individual grains. The identified particles are randomly assigned to 8 different material IDs. Interfaces of different IDs represent GBs. Further increasing the ID number did not yield any noticeable changes in cell performance. Details about the segmentation step can be found in the SI.

Simulation domain

Finally, we assemble a virtual cell for 3D simulations consisting of a planar isotropic anode, electrolyte separator layer, composite cathode, and current collectors on both electrodes. To reduce the computational cost of the structure-resolved simulations, we increase the voxel size of the cathode microstructures by a factor of 2. In this study we focus on structural properties of the composite cathode and, thus, assume a homogeneous electrolyte pellet as separator without pores and grain boundaries. A schematic of the simulation domain is shown in Figure S2.

Electrochemical simulations

Simulation framework

In this study, we use the Battery and Electrochemistry Simulation Tool BEST for the electrochemical simulations.[46] BEST is developed in a joint effort between Fraunhofer ITWM and DLR and has previously been adopted for the investigation of different ASSBs.[31,32,38,39] The governing equations are given by a set of coupled partial differential equations for the electrolyte and active material phase and can be derived from the conservation equations for mass and charge.[47,48] A summary of constitutive equations is given in Table S3.

An important aspect of this work is the effect of GBs on cell performance. GBs are known to contribute significantly to the electrolyte resistance of polycrystalline LLZO and affect the charge transport across the electrodes.[18,38] In our simulations different grains are identified by the material IDs assigned in the segmentation step (cf. Microstructure generation and virtual cell assembly). We calculate the current between different grains using a Butler-Volmer-like approach introduced by Neumann et al. [Eq. (1)].[38]

$$i_{GB} = i_0^{GB}\left[\exp\left(\frac{\Delta\tilde{\varphi}}{2RT}\right) - \exp\left(-\frac{\Delta\tilde{\varphi}}{2RT}\right)\right] \quad (1)$$

The current density depends on the local difference in electrochemical potential $\Delta\tilde{\varphi}$ at the interface between two adjacent grains. The GB resistance is linked to the exchange current density i_0^{GB} which can be estimated from electrochemical impedance spectroscopy (EIS) measurements.[38]

Material parameters

The focus of this work is on the effect of composite cathode geometry and material properties on cell performance. Parameters of the electrochemical simulations are taken from the literature and are listed in Table 1.

Research Article
doi.org/10.1002/batt.202300167
Chemistry Europe
European Chemical Societies Publishing

Table 1. Parameters of the electrochemical simulations. Functional parameters are indicated by * and are given at initial conditions.

Symbol	Value	Unit	Short description	Ref.
Li-metal				
U_0^{AN}	0	V	Open circuit potential	–
σ_{Li}^{AN}	1	S/cm	Electronic conductivity	–
i_0^{Li}	2.59×10^{-2}	A/cm^2	Exchange current density	[38]
α^{Li}	0.5	–	Symmetry factor	–
LLZO				
c_{Li}^{SE}	0.0384	mol/cm^3	Concentration of Li-ions	[38]
κ_{Li}^{SE}	7.69×10^{-4}	S/cm	Li-ion bulk conductivity	[38]
D_{Li}^{SE}	5.36×10^{-9}	cm^2/s	Li-ion diffusion coefficient	[38]
t_{Li}^{+}	1	–	Transference number	–
i_0^{GB}	6.91×10^{-3}	A/cm^2	GB exchange current density	[38]
C_{DL}^{GB}	9.75×10^{-9}	F/cm^2	GB double layer capacity	[38]
l_{sep}	25	µm	Separator thickness	–
LCO				
U_0^{CAM}	4.2	V	Open circuit potential*	[56]
$c_{Li}^{CAM,0}$	0.027058	mol/cm^3	Initial concentration of Li-ions	[31]
$c_{Li}^{CAM,max}$	0.051555	mol/cm^3	Maximum concentration of Li-ions	[57]
σ_{Li}^{CAM}	4.47	S/cm	Electronic conductivity*	[58]
D_{Li}^{CAM}	8.48×10^{-12}	cm^2/s	Li-ion diffusion coefficient*	[59]
i_{00}^{CAM}	0.0116	$\frac{Acm^{2.5}}{mol^{1.5}}$	Exchange current density factor	Calc. from [54]
α^{Li}	0.5	–	Symmetry factor	[31]
Boundaries				
il	1	mA/cm^2	Discharge current density	–
U_{cut}	3.4	V	Cut-off voltage	–

Solid electrolyte

The solid electrolyte is treated as a single ion conductor with a transference number of 1.[49,50] This implies that Li-ions move exclusively due to migration in the electric field and no concentration gradients form in the electrolyte phase. However, grain boundaries in the electrolyte limit the effective ionic conductivity. Neumann et al.[38] parameterized their GB model by comparing simulated impedance spectra with EIS data.[51] The reported GB exchange current density of $i_0^{GB} = 6.91 \cdot 10^{-3}$ A/cm^2 results in a corresponding resistance per GB of approximately $R_{GB} = 3.7\ \Omega\,cm^2$.

Cathode active material parameters

Parameters determining the electrochemical properties of the CAM are open circuit voltage, Li-ion diffusion coefficient, and electrical conductivity. These parameters are given as function of Li-concentration reflecting changes in conductivity and Li-mobility. In the first part of the manuscript, the parameters used represent LCO. In the last section, parameters representing NMC811 are adopted from Refs. [36, 52, 53].

SE/CAM interface

The exchange current density i_0 at the SE/CAM interface is determined from EIS data reported in Ref. [54]. The authors measure a charge transfer resistance R_{CT} of 2600 $\Omega\,cm^2$. The exchange current density i_0 can be derived by linearizing the kinetic expression [Eq. (2)].[36,55]

$$i_0 = \frac{RT}{zFAR_{CT}} \tag{2}$$

Li-metal

Li-metal is assumed to be in ideal contact with the SE separator. Parameters are taken from Ref. [38].

Simulation setup

We use periodic boundary conditions at lateral boundaries of our simulation domain and apply a constant discharge current density of 1 mA/cm^2 in all simulations. This value falls within the range of reported critical current densities for garnet-type

electrolytes in contact with Li-metal anodes.[60] At lower current densities, local currents and overpotentials are generally lower, resulting in reduced sensitivity to microstructural variations. The simulations are stopped after reaching the lower cut-off voltage of 3.4 V.

Definition of performance indicators and characteristic properties

Geometric characteristics

First, structural properties of the composite cathode were extracted from the microstructures, including the active surface area, connectivity, and tortuosity.

Solid volume fraction

In order to compare structures with different active material fractions, we use the solid volume fraction SVF_{CAM} [Eq. (3)].

$$SVF_{CAM} = \frac{V_{CAM}}{V_{CAM} + V_{SE}} \tag{3}$$

In this context, SVF_{CAM} gives the ratio of active material volume to the total solid volume and, thus, is independent of porosity.

Active area

The active area was determined by calculating the number of neighboring SE and CAM voxel surfaces using a Euclidean distance transform on the microstructure data.[61]

Connectivity

The connectivity of the SE and CAM phase was calculated from the number of isolated SE and CAM voxels $n_{iso,j}$ and the total number of voxels of the respective phase $n_{tot,j}$ [Eq. (4)].

$$Connectivity = 1 - \frac{n_{iso,j}}{n_{tot,j}} \tag{4}$$

Isolated SE clusters include electrolyte particles that are not connected to the separator and do not contribute to the ionic conduction network. Similarly, isolated active material particles are not connected to the cathode current collector. Before starting the electrochemical simulations, isolated clusters were removed from the input structure to improve numerical stability.

Effective conductivity

The effective partial conductivities and tortuosities of the CAM and SE phase were calculated by solving the Poisson equation. For an applied voltage difference of $U = 1$ V at the boundaries of the composite cathode structure, the resulting current density j was determined separately for the SE or CAM network, respectively. This enables the evaluation of the effective partial ionic and electric conductivity [Eq. (5)].

$$\sigma_{eff,i} = l \cdot \frac{j}{U}, \tag{5}$$

where l is the thickness of the sample in direction of the applied voltage difference. The tortuosity τ_i is calculated from the bulk conductivity σ_i and volume fraction ε_i of the respective material [Eq. (6)].[62]

$$\tau_i = \sqrt{\frac{\sigma_i}{\sigma_{eff,i}}} \cdot \varepsilon_i \tag{6}$$

Electrochemical characteristics

The most important electrochemical properties in our study are the capacity and specific energy of the electrode and cell, respectively.

Capacity

Based on the simulated discharge curves we evaluate the gravimetric capacity of the CAM at the lower cutoff voltage of 3.4 V according to Eq. (7):

$$C_{grav} = \frac{C_{3.4V}}{V_{CAM} \cdot \rho_{CAM}}, \tag{7}$$

where V_{CAM} and ρ_{CAM} are the volume and density of CAM, respectively. $C_{3.4V}$ is the capacity in mAh at 3.4 V. In order to provide comparable data, C_{grav} can be normalised with the theoretical capacity $C^{theo}_{grav,Ca}$ of the cathode structure [Eq. (8)].

$$C^{theo}_{grav,Ca} = \frac{\left(c^{CAM,max}_{Li} - c^{CAM,0}_{Li}\right)F}{\rho_{CAM}} \tag{8}$$

The normalized capacity $C_{norm} = C_{grav}/C^{theo}_{grav,Ca}$ can be interpreted as the average utilization of the CAM in the electrode.

Specific energy

Specific energy E_{grav} of the cell is calculated per mass of anode, separator and cathode [Eq. (9)].

Research Article
doi.org/10.1002/batt.202300167
Chemistry Europe
European Chemical Societies Publishing

$$E_{grav} = \frac{\int_{t_0}^{t_{end}} i \cdot U dt}{m_{An} + m_{Sep} + m_{Ca}} \quad (9)$$

The mass of the separator and cathode is determined based on the microstructure used as input for the simulation. We assume an ideal balancing of negative and positive electrode (n/p = 1) and neglect the weight of current collectors and cell housing. The corresponding anode mass is then given by Eq. (10).

$$m_{An} = \frac{C^{theo}_{grav,Ca} \cdot m_{CAM}}{C^{theo}_{grav,Li}} \quad (10)$$

The material parameters used for the calculation of gravimetric capacity and energy density are listed in Table S4.

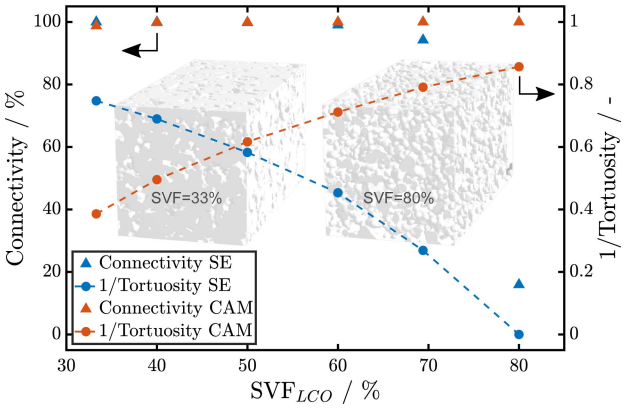

Figure 2. Influence of the solid volume fraction of LCO on connectivity and tortuosity of the electrolyte network. Note that the inverse of tortuosity is shown. The density after sintering and mean initial particle diameters are constant at $\rho_S = 93.1\,\%$, $d_{CAM} = 2.00\,\mu m$ and and $d_{SE} = 1.41\,\mu m$. The discharge simulations were conducted at a current density of 1 mA/cm^2. The inset shows the SE phase for $SVF_{LCO} = 33.3\,\%$ and $SVF_{LCO} = 80.0\,\%$.

Results and Discussion

In this section, we analyze the relevant parameters determining composite cathode performance. Processes in the electrode are coupled and several requirements must be met to maximize cathode utilization.[17] An important aspect is the optimization of the composite cathode microstructure depending on the properties of solid-solid-interfaces and bulk transport parameters. The aim of this study is to identify the relevant properties for an advantageous cathode design by considering the CAM fraction, density, and particle sizes in a LCO/LLZO composite cathode. As illustrated in Figure 1, we calculate geometrical characteristics from the unsegmented cathode structures, while additionally taking into account GBs in the electrochemical simulations. Finally, we extend our study to the state-of-the-art CAM NMC811, investigating the impact of CAM properties on optimal electrode design and providing an outlook for future cathode chemistries in ASSBs. When mentioning NMC in this manuscript, we specifically refer to NMC811 as the CAM investigated in our study.

Influence of the CAM fraction

Structural analysis

The microstructure and properties of the SE and CAM phase determine the performance of the cathode. Relevant parameters are the composition, connectivity and tortuosity of each phase. These are strongly influenced by the CAM fraction, that determines the ionic and electronic 3D transport network.[63]

Figure 2 shows the connectivity and tortuosity of 3D transport networks as function of CAM fraction. Red and blue triangles give the connectivity of the CAM and electrolyte, respectively, while the inverse of tortuosity for both phases is shown using dashed lines.

At small LCO fractions, the connectivity of the CAM phase decreases. An increasing number of CAM particles are not connected to the current collector and, thus, are electrochemically inactive. However, above $SVF_{LCO} = 33.3\,\%$, considered as lower limit in this study, the effect is not pronounced. For even smaller CAM fractions, a significant decrease in connectivity and, hence, capacity is expected. Both smaller connectivity and reduced CAM content contribute to a higher tortuosity in the CAM phase and reduced effective electronic conductivity.

On the other hand, high LCO fractions lead to an increase in tortuosity and a decrease in connectivity of the SE phase. Above $SVF_{LCO} = 70\,\%$, there is no longer a percolating network for ion transport and the amount of SE particles connected to the separator reduces to less than 20 %. This will cause a significant drop in electrode capacity as only CAM particles close to the separator can be lithiated. CAM particles that are not connected to the separator are not accessible to Li-ions, rendering them electrochemically inactive. At the same time, the tortuosity of the electrolyte network increases at high CAM fractions, reducing the effective ionic conductivity which has a negative impact on cell impedance and CAM utilization.

Figure 3 shows the effect of the CAM fraction on the calculated, normalized partial conductivities of the composite cathode. Red dots represent the results of the effective conductivity simulations. Decreasing SE fractions lead to a reduction of the effective ionic conductivity due to the higher tortuosity and lower connectivity discussed above. Similarly, lower CAM fractions result in smaller effective electronic conductivities. Finally, we can identify limiting SE and CAM fractions, below which the effective conductivity drops to 0 due to a loss of percolation in the respective phase. Our calculations indicate that the limiting material fraction is around 20 vol.% for both the SE and CAM.

Figure 3 includes the experimental data from Minnmann et al. (blue squares) measured on NMC622/Li_6PS_5Cl composite cathodes.[22] The simulations are in qualitative agreement with the experiments. However, the simulated conductivities are slightly higher for both ion and electron transport. Nonetheless, the limiting volume fractions relevant for cell design are in the same range indicating that structural limitations are reprodu-

Research Article
doi.org/10.1002/batt.202300167
Chemistry Europe
European Chemical Societies Publishing

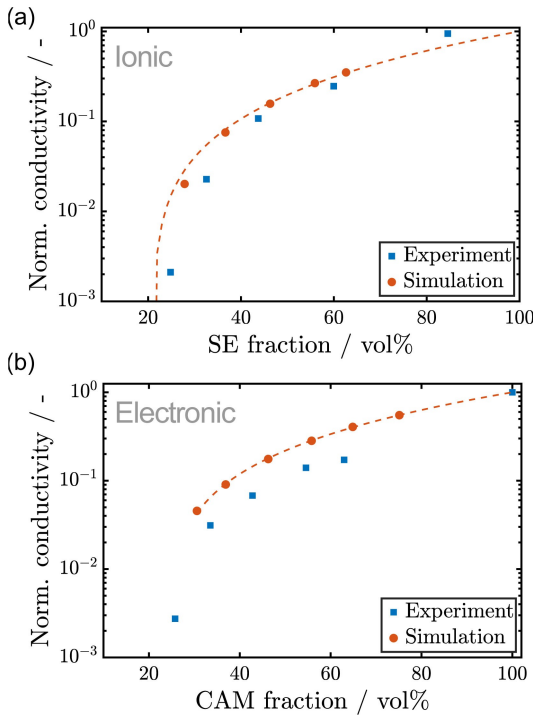

Figure 3. Influence of the cathode composition on the partial effective conductivities of the composite cathode and comparison to the experimental data from Minnmann et al.[22] Effective conductivity is normalized with bulk conductivity of SE and CAM, respectively. The density after sintering and mean initial particle diameters are constant at $\rho_S = 93.1\,\%$, $d_{CAM} = 2.00\,\mu m$ and $d_{SE} = 1.41\,\mu m$. (a) Effective ionic conductivity. (b) Effective electronic conductivity.

cible in our virtual structures. Other relevant properties affecting the conductivity are the electrode density, particle morphology, and contact resistance between particles, which deviate between data sets. Note that the simulations in this paragraph neglect GB effects and the effective ionic conductivity is mainly determined by the tortuosity of the electrolyte network. The good agreement between the simulations and the experimental data by Minnmann et al.[22] indicates a small GB resistance in Li_6PS_5Cl electrolyte. The effect of GBs in LLZO electrolyte is discussed in subsequent paragraphs. Systematic conductivity measurements on LLZO based composite electrodes are lacking in the literature and additional data is needed for quantitative validation of model predictions.

It's worth noting that while the effective electrical conductivity in the CAM phase decreases at low CAM fractions, the bulk conductivity of LCO is higher than the ionic conductivity in LLZO.[58,59] In fact, Figure S4 highlights that the effective electronic conductivity at low SOCs is orders of magnitude higher than the effective ionic conductivity. Therefore, kinetic limitations are mainly due to ion conduction.

Electrochemical analysis

In the previous section we focused on the connectivity and tortuosity of the SE and CAM phase neglecting the influence of particle contact. However, grain boundaries typically decrease the effective ionic conductivity in the SE. The GB resistance depends on the processing where densification and sintering have a significant impact on the resulting effective conductivity.[17,64]

Figure 4a illustrates the impact of GB resistance on the effective ionic conductivity and normalized capacity at different CAM fractions. We simulate four different cases with increasing GB resistance. In addition to assuming perfect contact between SE particles (Case: w/o GBs) and the high GB resistance reported in Ref. [38] (Case: $R_{GB,3}$), we also assume two intermediate cases. The GB exchange current densities ($7\cdot10^{-1}$ A/cm^2, $7\cdot10^{-2}$ A/cm^2, $7\cdot10^{-3}$ A/cm^2) correspond to local GB resistances of $R_{GB,1} = 3.6\cdot10^{-2}$, $R_{GB,2} = 3.6\cdot10^{-1}$ and $R_{GB,3} = 3.6\,\Omega\,cm^2$, respectively.

As GB resistance increases, the simulated effective ionic conductivity of the virtual structures drops accordingly. For the highest GB resistance $R_{GB,3}$, the effective conductivity is approximately two orders of magnitude smaller than in the simulation case with perfect inter-particle contact. The red to orange lines in Figure 4a show the corresponding normalized capacities. In case of negligible GB resistance, the maximum normalized capacity is close to 0.9 indicating good utilization of the CAM. The capacity reaches a maximum for a solid volume fraction of LCO around 40 % and decreases at high and low CAM fractions. This is a result of the loss of connectivity and increasing tortuosity at extreme compositions discussed above. At $SVF_{LCO} = 80\,\%$ the normalized capacity drops to almost zero due to the loss of a percolating network since only particles close to

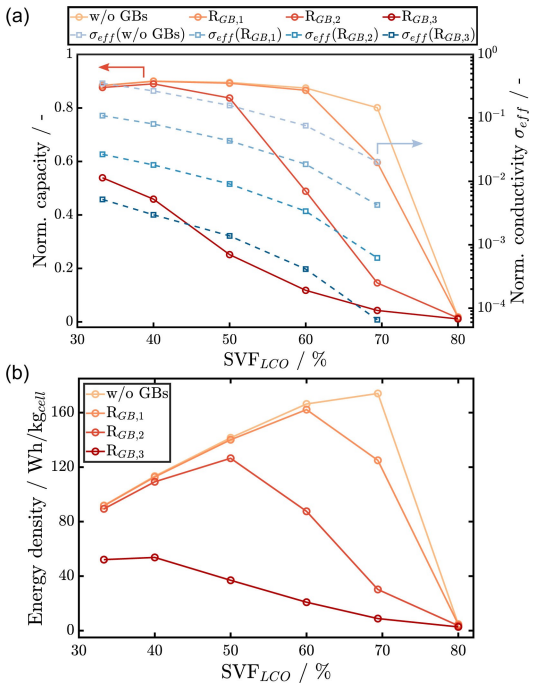

Figure 4. Influence of the grain boundary resistance on the (a) effective ionic conductivity and normalized capacity and (b) energy density. $R_{GB,1} = 3.6\cdot10^{-2}\,\Omega\,cm^2$, $R_{GB,2} = 3.6\cdot10^{-1}\,\Omega\,cm^2$, $R_{GB,3} = 3.6\,\Omega cm^2$. The density after sintering and mean initial particle diameters were constant at $\rho_S = 93.1\,\%$, $d_{CAM} = 2.00\,\mu m$ and $d_{SE} = 1.41\,\mu m$. The discharge simulations were conducted at a current density of 1 mA/cm^2.

Research Article
doi.org/10.1002/batt.202300167

the separator can be lithiated. Note that despite the increasing tortuosity of the SE towards higher CAM contents the effect on normalized capacity is not pronounced. This indicates that the ionic conductivity of LLZO for small GB contributions is sufficient for operation at moderate current densities.

Increasing GB resistance has a significant effect on the normalized capacity. Generally, the capacity decreases with increasing GB resistance and CAM content as a result of a reduced effective ionic conductivity. At the same time, the maximum capacity shifts towards structures with lower LCO fractions. Electrodes with lower tortuosity are needed to compensate the effect of increasing GB resistance. Interestingly, for the GB resistance reported in Ref. [38] the virtual structure with $SVF_{LCO} = 30\,\%$ performs best in terms of normalized capacity. This result demonstrates that electrode design and process development determining material and interface properties cannot be done independently.

Figure 5a visualizes the effect of GB resistance on CAM utilization in an electrode with $SVF_{LCO} = 50\,\%$. The results of discharge simulations were used to calculate histograms of Li stoichiometry in each CAM voxel. Additionally, the inset shows the average CAM utilization across the cathode, which was determined by calculating the normalized capacity for every slice of the cathode geometry. While the average CAM utilization provides insights into the limitations of ionic transport at the electrode level, the histogram provides additional information, such as limiting diffusion in CAM particles at the particle level.

In the case of negligible GB resistance (w/o GBs), the CAM shows a high Li content and a uniform utilization. In the histogram the majority of CAM voxels has a Li content between 0.9 an 0.98. Voxels close to the separator are almost completely lithiated. On the other hand, voxels in the center of the particles are closer to a Li content of 0.9 due to slow diffusion in the CAM. It's important to note that in the histogram, the blue and red bars describing the w/o GBs and $R_{GB,1}$ cases overlap significantly due to the small influence of $R_{GB,1}$ on cell performance. In the $R_{GB,2}$ case, the increasing GB resistance results in a decrease in ionic conductivity in the SE phase. This leads to a reduction in CAM utilization across the length of the cathode. The higher ionic resistance of the SE phase results in a steeper gradient in CAM utilization and higher average utilization of particles closer to the separator, compared to the $R_{GB,1}$ case. However, CAM utilization closer to the current collector is significantly reduced. As a result, in the histogram, more voxels show a lower Li-content. In the $R_{GB,3}$ case, the histogram shows a large portion of voxels close to the initial Li concentration at the end of the discharge simulation. In the spatial distribution across the electrode thickness we can observe that the utilization of the CAM decreases significantly from separator to current collector. A large portion of the CAM close to the current collector is effectively not lithiated and does not contribute to the cell capacity.

This is also shown in the 3D images in Figure 5b that illustrate the lithium distribution in the CAM at the cut-off voltage. Due to the low effective ionic conductivity in the $R_{GB,3}$ case, Li-ions are not able to lithiate CAM particles away from the separator. This effectively reduces the active thickness of the electrode resulting in higher local reaction currents at the CAM-SE interfaces in the region adjacent to the separator. The slow Li diffusion in the CAM leads to Li accumulation on CAM particle surfaces causing a rapid drop in cell voltage at a higher current (cf. Figure S5). This highlights the importance of fast ion transport for cathode designs targeting high energy density.[31]

The trade-off between high CAM content and CAM utilization is a key consideration in composite cathode design. Figure 4b shows the specific energy as function of CAM fraction in the composite. Generally, high CAM contents are necessary to achieve high specific energy. However, at the same time, transport limitations in the SE reduce the utilization of the CAM. With increasing GB resistance the effective ionic conductivity decreases, causing reduced CAM utilization and energy density. Consequently, the optimal LCO:LLZO ratio shifts towards lower values, indicating that a reduced tortuosity in the SE is necessary to counteract the high GB resistance. These correla-

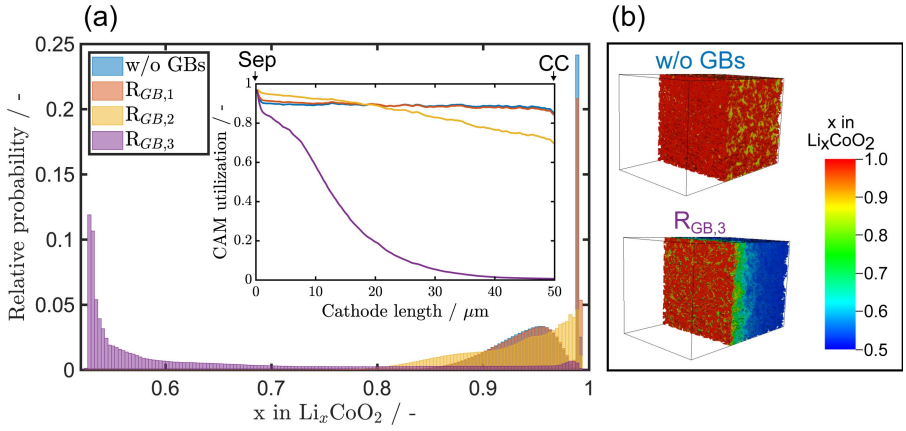

Figure 5. Influence of the GB resistance on the CAM utilization for a structure with LCO solid volume fraction of 50 %, a density after sintering of 93.1 % and mean initial particle diameters of $d_{CAM} = 2.00$ μm and $d_{SE} = 1.41$ μm. $R_{GB,1} = 3.6 \cdot 10^{-2}\ \Omega\,cm^2$, $R_{GB,2} = 3.6 \cdot 10^{-1}\ \Omega\,cm^2$, $R_{GB,3} = 3.6\ \Omega\,cm^2$. (a) Li content of the CAM voxels after the discharge at 1 mA/cm^2. The inset shows the mean normalized capacity across the cathode length. (b) The Li content of the CAM in the 3D-structure after the discharge at 1 mA/cm^2.

Research Article
doi.org/10.1002/batt.202300167
Chemistry Europe
European Chemical Societies Publishing

tions are also shown in Figure S6, which presents our simulation results in terms of total area specific capacity.

With regard to the influence of the CAM fraction on the electrochemical performance, we conclude that:

- The electrochemical performance at high CAM fractions is limited by the effective ionic conductivity and isolated electrolyte clusters.
- To achieve high CAM utilization at high CAM fractions, the GB resistance must not significantly exceed values measured in dense pellets.
- Simulations allow to derive an optimal electrode composition and thickness depending on transport properties and operation conditions.

Influence of the density after sintering

The sinter density of the composite cathode describes the residual porosity in the structure after manufacturing. In contrast to a conventional Li-ion battery with liquid electrolyte, pores cannot be completely filled by the solid electrolyte in an ASSB. While the presence of void space reduces the energy density, pores also contributes to increased tortuosity by blocking transport pathways. Additionally, low densities can result in a higher fraction of completely isolated particles that are electrochemically inactive and do not contribute to cell capacity. Small voids at the interface between SE and CAM particles reduce the active surface area and cause constriction effects.[65] Furthermore, residual pores in the electrolyte can impair its mechanical integrity.[66] The density after sintering is limited by the manufacturing process, which must be optimized to achieve high densification at reduced sintering temperatures.[67] Our simulation study aims to identify optimization potentials for cell manufacturing. However, it should be noted that pore formation and contact loss between individual particles can also result from mechanical degradation due to volume changes of the CAM during operation.[17] While our current model does not incorporate mechanics, our simulation results provide valuable insights into the impact of increasing porosity in the overall microstructure on cell performance. However, specific changes in the microstructure, such as pore formation during cycling, are beyond the scope of our current model.

Structural analysis

Figure 6 shows the impact of the density after sintering on the connectivity of the SE and CAM phase for three different cathode compositions (SVF_{LCO} = 33.3, 50.0 and 69.4 %). For all structures, an increase in porosity leads to a higher number of electrochemically inactive particles. For low CAM fractions (SVF_{LCO} = 33.3 %), this primarily affects the CAM phase, while cathodes with high CAM fractions (SVF_{LCO} = 69.4 %) show low connectivity in the SE phase at reduced sinter densities. As porosity increases, both ionic and electrical transport pathways collapse, leading to a decline in connectivity. A higher number

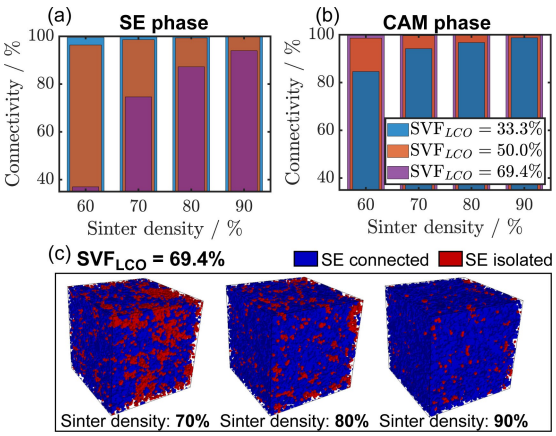

Figure 6. Influence of the density after sintering on the connectivity in the (a) SE phase and (b) CAM phase for SVF_{LCO} = 33.3, 50.0 and 69.4 %. (c) The influence of the density after sintering on the connectivity in the SE phase for the 3D composite cathode structure with SVF_{LCO} = 69.4 %. The mean initial particle diameters were constant at d_{CAM} = 2.00 µm and d_{SE} = 1.41 µm.

of inactive CAM particles decreases the cell capacity. Additionally, reduced connectivity in the SE phase impedes ionic transport, resulting in a poor rate capability. Figure 6c gives a visual impression of the number of isolated SE clusters shown in red color. The separator is to the left and the current collector to the right of each microstructure image. The share of unconnected clusters increases with increasing distance from the separator. Thus, CAM particles close to the current collector are more likely to show reduced utilization at low densities and high CAM fractions.

Figure 7 shows the influence of the density after sintering on the tortuosity in the SE phase as well as the active area between SE and CAM. A lower density results in a higher number of isolated SE clusters and inter-particle pores, which leads to an increase in tortuosity. Generally, we observe an exponential increase of tortuosity with decreasing density in

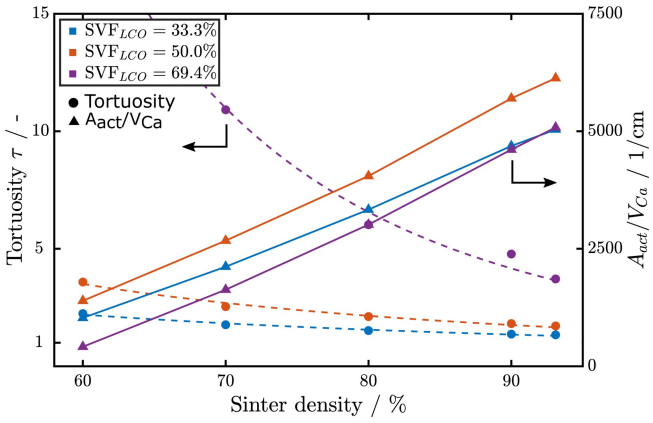

Figure 7. Influence of the density after sintering on the tortuosity in the SE phase and the active interface area between SE and CAM for SVF_{LCO} = 33.3, 50.0 and 69.4 %. Isolated material clusters were removed from the structures before computing the active area. The mean initial particle diameters were constant at ρ_S = 93.1 %, d_{CAM} = 2.00 µm and d_{SE} = 1.41 µm.

Research Article
doi.org/10.1002/batt.202300167
Chemistry Europe
European Chemical Societies Publishing

the sintered state. This effect is especially prominent for structures with a high LCO fraction (SVF_{LCO} = 69.4 %). Even at the maximum density (93.1 %) the configuration with high CAM fraction shows higher tortuosity than compositions with elevated LLZO content and low sinter density. As the void fraction increases, the ionic pathways are further compromised until, eventually, the percolating network for ion transport breaks down.

Besides, the additional voids at the SE/CAM interface lead to a decrease in active area. This results in an inhomogeneous distribution of local currents, higher overpotentials and, ultimately, a decrease in capacity. The structure with SVF_{LCO} = 50 % shows the highest active area since a similar share of SE particles is in direct contact with the CAM. We observe almost linear dependence of the surface area on density after sintering. Moreover, the effect of cathode composition on active area is minor compared to the significant effect on tortuosity observed at low densities.

Electrochemical analysis

Finally, Figure 8 illustrates the impact of density after sintering on the electrochemical characteristics for different LCO fractions. We investigate two scenarios, one with negligible grain boundary resistance (w/o GBs) and another with high grain boundary resistance (w/ GBs) as per Ref. [38].

Figure 8a shows the normalized electrode capacity. Generally, low densities reduce the electrode capacity due to isolated clusters, higher tortuosity, and smaller active areas. For the scenario with negligible GB resistance, the structure with SVF_{LCO} = 50 % provides the highest capacity for all densities. This indicates that the optimal cathode composition does not significantly depend on density after sintering. The high GB resistance scenario leads to a significant reduction in capacity for all structures. In that case, maximum normalized capacities are reached for small CAM fractions (SVF_{LCO} = 33.3 %) that provide reduced tortuosity in the SE phase. In electrodes with high CAM content even a moderate increase in porosity is not tolerable resulting in almost negligible capacity.

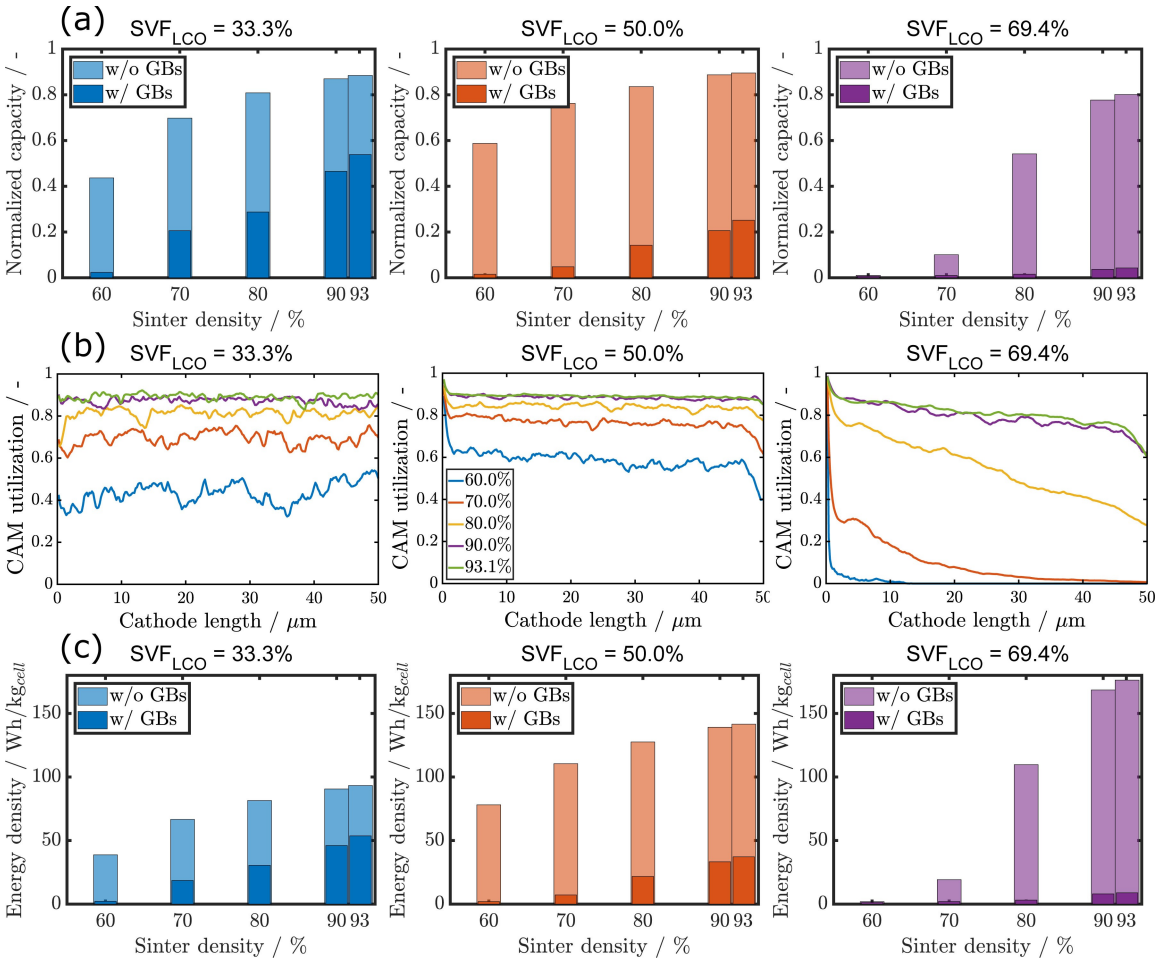

Figure 8. (a) Influence of the density after sintering on the simulated gravimetric capacity for different CAM fractions and the simulation cases with neglible GB resistance (w/o GBs) and high GB resistance (w/ GBs) of $R_{GB,3}$ = 3.6 Ω cm². (b) Mean CAM utilization over the cathode length for different densities after sintering and the simulation case w/o GBs. (c) Influence of the density after sintering on the simulated energy density for different CAM fractions for the simulation cases w/o GBs and w/ GBs. The mean initial particle diameters were constant at d_{CAM} = 2.00 μm and d_{SE} = 1.41 μm. The discharge simulations were conducted at 1 mA/cm².

Research Article
doi.org/10.1002/batt.202300167
Chemistry Europe
European Chemical Societies Publishing

Figure 8b shows the influence of the cathode density on the mean utilization along the cathode length for the simulation case with negligible GB resistance. For $SVF_{LCO}=33.3\,\%$, the CAM is lithiated uniformly even at the lowest assumed cathode density. However, at $SVF_{LCO}=69.4\,\%$, particles further away from the separator show a reduced utilization. As density decreases, the drop in capacity along the cathode length becomes more pronounced. This result emphasizes that insufficient effective ionic conductivity impedes higher utilization of the CAM.

As shown in Figure 8c, the cathode density has a significant impact on energy density. At low grain boundary resistance, energy density is maximum for $SVF_{LCO}=69.4\,\%$ at densities above 90 %. However, at 80 % density, cathodes with $SVF_{LCO}=50\,\%$ already outperform those with $SVF_{LCO}=69.4\,\%$. This highlights the importance of high density after sintering in achieving high energy density cathodes. At high grain boundary resistance, the maximum energy density is observed for the structure with $SVF_{LCO}=33.3\,\%$ across all densities, owing to the reduced tortuosity in the SE phase.

In summary, low cathode densities negatively impact cell performance by decreasing connectivity, reducing the active area, and increasing tortuosity. These factors decrease the effective ionic conductivity, which is particularly detrimental for electrodes with high CAM fraction.

Influence of the SE and CAM particle size

Both the particle or grain size of the CAM and SE are determined by the pretreatment and sintering during manufacturing. Suitable milling parameters and thus, particle sizes, are crucial for optimization of the composite cathode microstructure and performance.[22,29] The final particle morphology forms during the high-temperature sintering process, which induces grain growth and densification.[68,69] This is mimicked by a geometrical sintering in our structure generation algorithm that increases the size of individual particles. In our description of simulation results we refer to the mean particle diameter before sintering, which can be interpreted as the particle size of the starting powders. The segmentation of the SE phase after the geometrical sintering, which is the basis for the grain boundary model, gives slightly different values. Particle sizes resulting from the segmentation step and the corresponding particle size distributions are provided in Table S2 and Figure S3, respectively.

Structural analysis

Figure 9 shows the influence of the SE and CAM particle size on the calculated active area and geometrical tortuosity at $SVF_{LCO}=50\,\%$. A maximum contact area between SE and CAM can be achieved for the combination of small SE and CAM particle diameters (Figure 9a). However, at constant SE particle size, small CAM particles cause tortuous pathways in the SE due to the higher number of particles and thus, obstacles.[23] Low

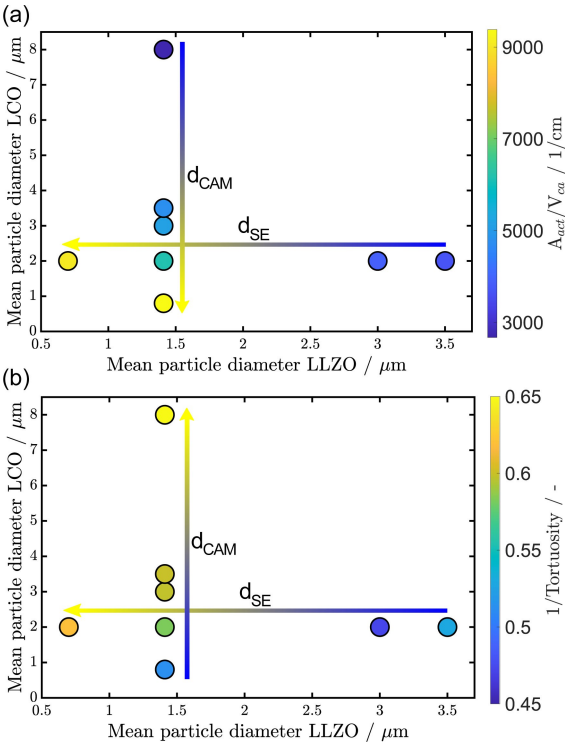

Figure 9. Influence of the particle size of LCO and LLZO on the geometric properties of the cathode structure: (a) Active area between LCO and LLZO. (b) Tortuosity in the SE phase. Solid volume fraction and density after sintering were constant at $SVF_{LCO}=50\,\%$ and $\rho_S=93.1\,\%$. Arrows indicate the optimal particle diameter for achieving maximum active area and tortuosity, respectively.

tortuosities are realized (Figure 9b) by small SE particles and moderate or large CAM particle size.

In this respect the particle size ratio $\lambda=d_{CAM}/d_{SE}$ is an important parameter, which has a significant impact on the geometrical properties of the composite cathode. To achieve short ionic pathways and good connectivity, SE particles must be smaller than CAM particles.[24,35] As λ increases, channels form between larger CAM particles that can be occupied by smaller SE particles. However, large CAM particles result in long diffusion pathways in the active material. Additionally, small SE particles increase the GB resistance. Both effects have a negative impact on electrode performance requiring careful balancing in electrode design.[21]

Electrochemical analysis

The size of particles and grains in the composite cathode plays a crucial role in determining the electrochemical performance of the cell. In addition to the tortuosity and active area it also influences the number of grain boundaries. A balance between these factors is essential to maximize the utilization of the CAM. Figure 10 illustrates the effect of the SE and CAM particle size on normalized capacity. It is important to note that the optimal particle size also depends on the grain boundary resistance in

Research Article
doi.org/10.1002/batt.202300167
Chemistry Europe
European Chemical Societies Publishing

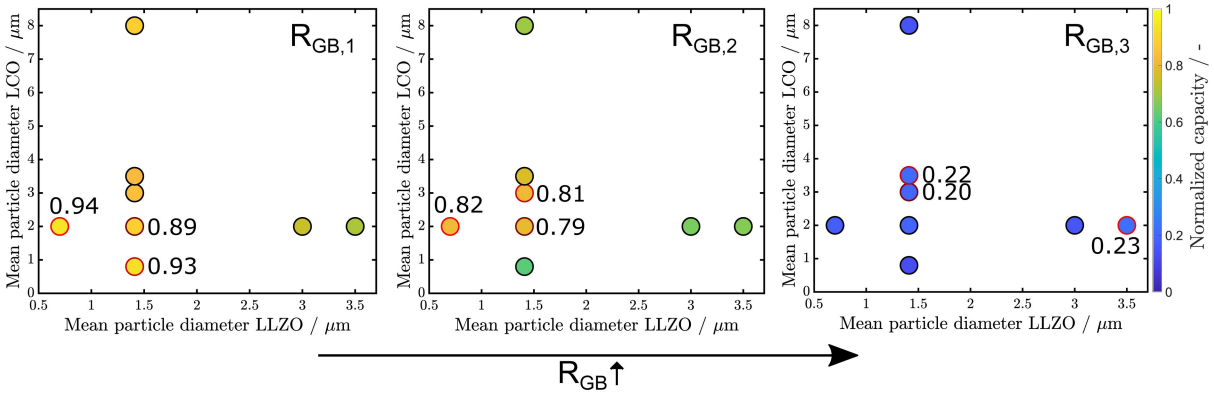

Figure 10. Influence of the grain boundary resistance on the gravimetric capacity for different LCO and LLZO particle sizes. $R_{GB,1} = 3.6 \cdot 10^{-2}\ \Omega\,cm^2$, $R_{GB,2} = 3.6 \cdot 10^{-1}\ \Omega\,cm^2$, $R_{GB,3} = 3.6\ \Omega\,cm^2$. For each simulation case the three highest capacities are highlighted with red circles. Solid volume fraction and density after sintering were constant at $SVF_{LCO} = 50\,\%$ and $\rho_S = 93.1\,\%$. The discharge simulations were conducted at 1 mA/cm^2.

the electrolyte. In our study we consider the cases $R_{GB,1}$–$R_{GB,3}$, spanning over two orders of magnitude.

In case of a small GB resistance, structures with both small CAM and SE particles provide the best electrochemical performance. These structures have a high active area, allowing for efficient charge transfer at the SE/CAM interface. Additionally, the short diffusion length in the CAM enables high utilization of the CAM particles. The increased tortuosity resulting from small CAM particles does not significantly impact cell performance since ion transport is not limiting electrode performance in this case.

However, as grain boundary resistance increases, the effective ionic conductivity in the SE decreases. As a result, configurations with lower tortuosity are favorable. In the $R_{GB,2}$ case maximum capacities are achieved with small SE particles and moderate CAM diameters ($d_{SE} = 0.8$ μm and $d_{CAM} = 2.0$ μm). While even smaller tortuosities can be obtained with larger CAM particles ($d_{SE} = 1.4$ μm and $d_{CAM} = 8.0$ μm), the longer diffusion length in the CAM has a negative impact on the utilization of the active material.

In the $R_{GB,3}$ case, the low effective ionic conductivity in the SE results in very low capacities. Structures with small SE particles have high active areas and low tortuosities, but the high number of SE particles increases the number of grain boundaries. For that reason, the structure with larger LLZO particles ($d_{SE} = 3.5$ μm and $d_{CAM} = 2.0$ μm) performs slightly better than the other configurations. Interestingly, high capacities can still be achieved at moderate GB resistance. However, in the $R_{GB,3}$ case the cell performance decreases significantly regardless of particle configuration and electrode composition. This indicates an upper limit of a tolerable GB resistance between $R_{GB,2}$ and $R_{GB,3}$ which is a strict requirement to be met in process development.

The trends and conclusions regarding the effect of particle size on electrochemical performance, as discussed for $SVF_{LCO} = 50\,\%$, should hold true for other cathode compositions as well. However, we anticipate that the optimization of effective ionic conductivity via particle size, achieved through both low tortuosity and GB resistance in the SE phase, becomes more significant at higher CAM volume fractions where ionic transport limitations are dominant.

To summarize, the choice of SE and CAM particle size influences a number of competing processes:

- Improved charge transfer kinetics and high active area is achieved with a combination of small SE and CAM particles.
- Smaller CAM particles provide short diffusion pathways, which are crucial for high CAM utilization.
- Low tortuosities are obtained at large particle size ratios λ.
- The effective ionic conductivity can be improved by increasing the SE particle size and thus reducing the number of GBs.

The optimal particle size and particle size ratio depends on the composition of the composite cathode and GB resistance. The design study given above provides guidelines for electrode design. However, for quantitative optimization material parameters, processing and operation conditions also have to be taken into account. Please note that, in addition to the mean particle size, the particle size distribution (PSD) influences the aforementioned effects and, consequently, impacts cell performance.

Influence of CAM properties

In order to increase the energy density, intensive research is focusing on the development of composite cathodes with novel CAMs that possess superior gravimetric capacity. State-of-the-art in Li-ion batteries are Ni-rich materials such as $LiNi_xCo_yAl_zO_2$ (NCA) and $LiNi_xMn_yCo_zO_2$ (NMC).[70] In this section we investigate the effect of CAM material parameters on electrode design.

NMC material properties

Replacing LCO with NMC is considered as a promising step towards high-capacity cathodes in garnet-based ASSBs.[15,17] However, the material properties of NMC also affect the optimal cell design. In this section we compare the active materials NMC811 and LCO.

Research Article
doi.org/10.1002/batt.202300167
Chemistry Europe
European Chemical Societies Publishing

The relevant properties of the CAM in our model are the open circuit voltage U_0^{CAM}, specific capacity ($c_{Li}^{CAM,max}$), chemical Li diffusion coefficient D_{Li}^{CAM}, electric conductivity σ_{Li}^{CAM}, and the exchange current density i_0^{CAM} for intercalation kinetics given by charge transfer resistance. Material parameters and sources are summarized in Table 2. All other simulation parameters are the same as in the previous sections. Note that i_0^{NMC} is also the same as in the previous simulations with LCO. Generally, NMC exhibits low interfacial stability with LLZO, making it challenging to measure the charge transfer resistance of pristine interfaces experimentally.[15]

Two key parameters relevant for operation, especially at elevated rates, are the chemical diffusion coefficient and electrical conductivity. A comparison of the concentration dependent Li-ion diffusion coefficient[53] and electrical conductivity[52] of LCO and NMC can be found in Figure S7. Ruess et al. have shown that the effective chemical diffusion coefficient of NMC in an ASSB is orders of magnitude lower in comparison to a Li-ion battery with liquid electrolyte.[53] Fast effective Li transport in liquid electrolytes originates from microcracks in the particles which are invaded by electrolyte. A process which is impossible in combination with solid electrolytes. Additionally, NMC has a low electrical conductivity, especially at high lithiation states. Both parameters adversely affect battery performance, counteracting the effect of higher specific capacity.

Electrochemical analysis

Figure 11a compares the simulation results of LCO and NMC in terms of normalized and gravimetric capacity of the CAM. The active material fraction was varied between $SVF_{CAM} = 33.3\,\%$ and $SVF_{CAM} = 80\,\%$ assuming negligible grain boundary resistance. For all generated structures, the simulations with LCO show a better CAM utilization due to the superior Li diffusivity and electrical conductivity of the CAM. The corresponding measure is the normalized capacity. However, despite the low chemical diffusion coefficient and poor electrical conductivity (see Figure S7c) the more relevant gravimetric capacity is still higher for NMC cathodes. These results indicate that research on LLZO-based cell designs should aim at integrating NMC811 as active material.[15]

Finally, we analyze the effect of particle size on the performance of the NMC composite cathode. Figure 11b illustrates how particle size influences cell performance in NMC composite cathodes including the effect of GBs. For our simulations studies we select the GB cases with resistance $R_{GB,1}$ and $R_{GB,2}$. As shown previously, in the case of $R_{GB,3}$, the effective ionic conductivities are insufficiently small to achieve capacities that are practically relevant. For the case with moderate GB resistance $R_{GB,1}$, maximum capacities are attained at both small LLZO and NMC particle size. Similarly to the simulations with LCO (cf. Figure 10), the optimum configuration for the $R_{GB,2}$ case shifts towards structures with both a high active area and a

Table 2. CAM parameter set for the electrochemical simulations with NMC. Functional parameters are indicated by * and given at initial conditions.

	Symbol	Value	Unit	Ref.
NMC	U_0^{NMC}*	4.2	V	[36]
	$c_{Li}^{NMC,0}$	0.01131	$\frac{mol}{cm^3}$	Calc.
	$c_{Li}^{NMC,max}$	0.04903	$\frac{mol}{cm^3}$	Calc.
	σ_{Li}^{NMC}*	8.83×10^{-3}	$\frac{S}{cm}$	[52]
	D_{Li}^{NMC}*	8.71×10^{-13}	$\frac{cm^2}{s}$	[53]
	i_{00}^{NMC}	0.0116	$\frac{Acm^{2.5}}{mol^{1.5}}$	Calc. from [54]

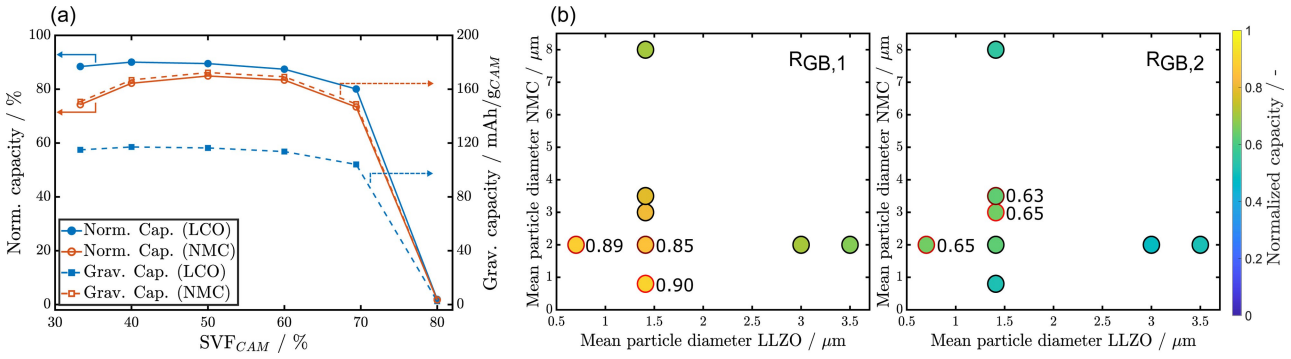

Figure 11. (a) Influence of the CAM parameters on the normalized and gravimetric capacity. The density after sintering and mean initial particle diameters were constant at $\rho_S = 93.1\,\%$, $d_{CAM} = 2.00\,\mu m$ and $d_{SE} = 1.41\,\mu m$. The discharge simulations were conducted at 1 mA/cm^2. (b) Influence of the grain boundary resistance on the gravimetric capacity for different NMC and LLZO particle sizes. $R_{GB,1} = 3.6\cdot10^{-2}\,\Omega\,cm^2$, $R_{GB,2} = 3.6\cdot10^{-1}\,\Omega\,cm^2$. For each simulation case the three highest capacities are highlighted with red circles. The solid volume fraction and density after sintering were constant at $SVF_{NMC} = 50\,\%$ and $\rho_S = 93.1\,\%$.

small tortuosity, as ionic transport becomes a limiting factor. Thus, trends and resulting design guidelines for the choice of particle sizes are similar as for LCO electrodes. However, compared to the simulations with LCO, normalized capacities are significantly lower, especially for the $R_{GB,2}$ case. The maximum normalized capacity is around 65% which corresponds to a specific capacity of around 133 mAh/g. Note that the capacity gain in comparison to the values of LCO (106 mAh/g) for the same electrolyte parameters is significantly lower than in case of negligible GB resistance, where capacities are at 172 mAh/g and 116 mAh/g for NMC811 and LCO, respectively (cf. Figure 11a). This result highlights that optimizing SE conductivity and particle size is crucial to achieve good utilization of NMC with lower Li chemical diffusion coefficient.

To further improve the utilization of NMC in composite cathodes, strategies such as reducing the CAM and SE particle size, using single-crystal NMC, and adding conducting additives can be employed.[17,71] These measures can counteract the low effective chemical diffusion coefficient of Li and improve the electrical percolation and conductivity of the composite cathode.

Conclusions and Outlook

The composite cathode plays a crucial role in determining the power and energy density of an all-solid-state battery. To improve the cell performance, the microstructure of the cathode must be optimized. In this article, we aim to identify guidelines for optimization by means of structure-resolved electrochemical simulations. Our model takes into account Li transport in the battery based on the conservation equations for mass and charge. A specific feature of our simulations is the modeling of transport resistances at grain boundaries in the solid electrolyte. By using input geometries that feature realistic morphologies of the solid electrolyte and active material, we can relate the electrochemical performance to the microstructural properties of the cathode. This allows us to study key design variables such as the active material fraction, density after sintering, and particle size.

To validate the results of our computational studies, it is important to perform corresponding experiments. As an initial step, impedance measurements for LCO/LLZO composite cathodes could be conducted to determine the ionic and electronic partial conductivities, similar to the approach used for thiophosphate electrolyte in a previous study.[22] Furthermore, more emphasis should be placed on conducting such measurements for different particle sizes and densities given their significant effects on charge transfer.

Our simulation results show that maximum capacities are achieved at moderate active material fractions in composite cathodes. Low active material fractions result in low effective electrical conductivity and reduced capacities, while high active material fractions lead to low effective ionic conductivity due to isolated clusters and tortuous pathways in the SE phase. To mitigate this, the composite cathode can be designed with a concentration-gradient approach, wherein the SE fraction is increased adjacent to the separator, and the CAM fraction is increased adjacent to the current collector. This design strategy potentially enables enhanced CAM utilization and improved energy density.[72,73] Additionally, low capacities can be attributed to high grain boundary resistances and small densities after sintering. To improve this, researchers should aim to reduce grain boundary resistance by adjusting manufacturing parameters and increase densities through new manufacturing techniques such as FAST/SPS.[67] The optimum particle size for maximum capacities is dependent on factors such as cathode composition, material parameters, and grain boundary resistance. Therefore, careful consideration should be given to particle size optimization for specific manufacturing routes. The use of NMC in solid-state-batteries has the potential to increase energy density, but also presents challenges in terms of ionic and electrical transport. Our simulations showed that LCO has superior Li mobility and electrical conductivity, leading to higher CAM utilization. However, NMC generally provides higher energy density due to ist larger gravimetric capacity. Due to lower NMC chemical diffusion coefficients NMC cathodes are more sensitive to low ionic conductivities which effectively increase local currents. To improve utilization of NMC, the composite cathode must be optimized by reducing particle size, using single-crystal NMC, and adding conducting additives for improved electrical conductivity. Ultimately, a balance must be struck between energy and power density through further optimization of transport properties and electrode designs. In addition, we believe that coupling electrochemical and mechanical models is essential for optimizing the composite cathode. This approach takes into account mechanical stress resulting from volume changes of the active material and could potentially alter optimal cathode designs.[15] Nevertheless, the simulation studies presented in this work provide guidelines for the development of ASSBs, as well as optimization strategies and protocols that can be readily applied to novel material systems.

Supporting Information

Additional references cited within the Supporting Information.[74,75]

Acknowledgements

The authors acknowledge support with computational resources provided by the state of Baden-Wurttemberg through bwHPC and the German Research Foundation (DFG) through grant no INST 40/575-1 FUGG (JUSTUS 2 cluster). We gratefully acknowledge the financial support by the German Federal Ministry of Research and Education (BMBF) within the scope of the FestBatt2 project (FKZ: 03XP0435A). Furthermore, we thank the German Federal Ministry for Economic Affairs and Climate Action (BMWK) for financial support as part of the OptiKeraLyt project (FKZ: 03ETE016C). This work was supported financially by the US Department of Energy (DOE) and the German Federal

Ministry of Education and Research (BMBF) through the CatSE^2 project (FKZ: 03XP0510D). Financial support from the BMBF under grant number 13XP0510A (CatSE^2) is gratefully acknowledged. Open Access funding enabled and organized by Projekt DEAL.

Conflict of Interests

There is no conflict of interest to declare.

Data Availability Statement

The data that support the findings of this study are available from the corresponding author upon reasonable request.

Keywords: all-solid-state batteries · composite cathode · continuum modeling · LLZO · microstructure-resolved simulation

[1] IEA, Energy Technology Perspectives 2020, Available at https://www.iea.org/reports/energy-technologyperspectives-2020, **2020**, accessed: 26 June 2023.
[2] Z. P. Cano, D. Banham, S. Ye, A. Hintennach, J. Lu, M. Fowler, Z. Chen, *Nat. Energy* **2018**, *3*, 279.
[3] M. Li, J. Lu, Z. Chen, K. Amine, *Adv. Mater.* **2018**, *30*, 1800561.
[4] M. Fichtner, K. Edström, E. Ayerbe, M. Berecibar, A. Bhowmik, I. E. Castelli, S. Clark, R. Dominko, M. Erakca, A. A. Franco, et al., *Adv. Energy Mater.* **2022**, *12*, 2102904.
[5] R. Wang, W. Cui, F. Chu, F. Wu, *J. Energy Chem.* **2020**, *48*, 145.
[6] Y. Zhang, T.-T. Zuo, J. Popovic, K. Lim, Y.-X. Yin, J. Maier, Y.-G. Guo, *Mater. Today* **2020**, *33*, 56.
[7] S. Nanda, A. Gupta, A. Manthiram, *Adv. Energy Mater.* **2021**, *11*, 2000804.
[8] J. Janek, W. G. Zeier, *Nat. Energy* **2016**, *1*, 1.
[9] Z. Wu, Z. Xie, A. Yoshida, Z. Wang, X. Hao, A. Abudula, G. Guan, *Renewable Sustainable Energy Rev.* **2019**, *109*, 367.
[10] R. Chen, Q. Li, X. Yu, L. Chen, H. Li, *Chem. Rev.* **2019**, *120*, 6820.
[11] X. Li, J. Liang, X. Yang, K. R. Adair, C. Wang, F. Zhao, X. Sun, *Energy Environ. Sci.* **2020**, *13*, 1429.
[12] C. Wang, K. Fu, S. P. Kammampata, D. W. McOwen, A. J. Samson, L. Zhang, G. T. Hitz, A. M. Nolan, E. D. Wachsman, Y. Mo, et al., *Chem. Rev.* **2020**, *120*, 4257.
[13] Z. D. Hood, Y. Zhu, L. J. Miara, W. S. Chang, P. Simons, J. L. Rupp, *Energy Environ. Sci.* **2022**, *15*, 2927.
[14] G. Vardar, W. J. Bowman, Q. Lu, J. Wang, R. J. Chater, A. Aguadero, R. Seibert, J. Terry, A. Hunt, I. Waluyo, et al., *Chem. Mater.* **2018**, *30*, 6259.
[15] C. Roitzheim, Y. J. Sohn, L.-Y. Kuo, G. Häuschen, M. Mann, D. Sebold, M. Finsterbusch, P. Kaghazchi, O. Guillon, D. Fattakhova-Rohlfing, *ACS Appl. Energ. Mater.* **2022**, *5(6)*, 6913–6926.
[16] K. J. Kim, J. L. Rupp, *Energy Environ. Sci.* **2020**, *13*, 4930.
[17] Y. Ren, T. Danner, A. Moy, M. Finsterbusch, T. Hamann, J. Dippell, T. Fuchs, M. Müller, R. Hoft, A. Weber, et al., *Adv. Energy Mater.* **2022**, page 2201939.
[18] S. Yu, D. J. Siegel, *Chem. Mater.* **2017**, *29*, 9639.
[19] X. Miao, S. Guan, C. Ma, L. Li, C.-W. Nan, *Adv. Mater.* **2022**, 2206402.
[20] G. Deysher, P. Ridley, S.-Y. Ham, J.-M. Doux, Y.-T. Chen, E. A. Wu, D. H. Tan, A. Cronk, J. Jang, Y. S. Meng, *Mater. Today Phys.* **2022**, page 100679.
[21] P. Minnmann, F. Strauss, A. Bielefeld, R. Ruess, P. Adelhelm, S. Burkhardt, S. L. Dreyer, E. Trevisanello, H. Ehrenberg, T. Brezesinski, et al., *Adv. Energy Mater.* **2022**, *12*, 2201425.
[22] P. Minnmann, L. Quillman, S. Burkhardt, F. H. Richter, J. Janek, *J. Electrochem. Soc.* **2021**, *168*, 040537.
[23] L. Froboese, J. F. van der Sichel, T. Loellhoeffel, L. Helmers, A. Kwade, *J. Electrochem. Soc.* **2019**, *166*, A318.
[24] T. Shi, Q. Tu, Y. Tian, Y. Xiao, L. J. Miara, O. Kononova, G. Ceder, *Adv. Energy Mater.* **2020**, *10*, 1902881.
[25] Y. J. Nam, D. Y. Oh, S. H. Jung, Y. S. Jung, *J. Power Sources* **2018**, *375*, 93.
[26] W. Zhang, D. A. Weber, H. Weigand, T. Arlt, I. Manke, D. Schröder, R. Koerver, T. Leichtweiss, P. Hartmann, W. G. Zeier, et al., *ACS Appl. Mater. Interfaces* **2017**, *9*, 17835.
[27] M. Cronau, A. Paulus, L. P. Pescara, M. Kroll, D. Renz, J. A. Mekontso, A. Marx, B. Roling, *Batteries & Supercaps* **2022**, *5*, e202200194.
[28] N. Kaiser, S. Spannenberger, M. Schmitt, M. Cronau, Y. Kato, B. Roling, *J. Power Sources* **2018**, *396*, 175.
[29] M. Cronau, M. Duchardt, M. Szabo, B. Roling, *Batteries & Supercaps* **2022**, *5(6)*, e202200041.
[30] F. Strauss, T. Bartsch, L. de Biasi, A.-Y. Kim, J. Janek, P. Hartmann, T. Brezesinski, *ACS Energy Lett.* **2018**, *3*, 992.
[31] M. Finsterbusch, T. Danner, C.-L. Tsai, S. Uhlenbruck, A. Latz, O. Guillon, *ACS Appl. Mater. Interfaces* **2018**, *10*, 22329.
[32] A. Neumann, S. Randau, K. Becker-Steinberger, T. Danner, S. Hein, Z. Ning, J. Marrow, F. H. Richter, J. Janek, A. Latz, *ACS Appl. Mater. Interfaces* **2020**, *12*, 9277.
[33] S. Randau, F. Walther, A. Neumann, Y. Schneider, R. S. Negi, B. Mogwitz, J. Sann, K. Becker-Steinberger, T. Danner, S. Hein, et al., *Chem. Mater.* **2021**, *33*, 1380.
[34] S. Yamakawa, S. Ohta, T. Kobayashi, *Solid State Ionics* **2020**, *344*, 115079.
[35] A. Bielefeld, D. A. Weber, J. Janek, *ACS Appl. Mater. Interfaces* **2020**, *12*, 12821.
[36] A. Bielefeld, D. A. Weber, R. Rueß, V. Glavas, J. Janek, *J. Electrochem. Soc.* **2022**, *169*, 020539.
[37] C. Park, S. Lee, K. Kim, M. Kim, S. Choi, D. Shin, *J. Electrochem. Soc.* **2019**, *166*, A5318.
[38] A. Neumann, T. R. Hamann, T. Danner, S. Hein, K. Becker-Steinberger, E. Wachsman, A. Latz, *ACS Appl. Energ. Mater.* **2021**, *4*, 4786.
[39] T. Ates, A. Neumann, T. Danner, A. Latz, M. Zarrabeitia, D. Stepien, A. Varzi, S. Passerini, *Adv. Sci.* **2022**, *9(18)*, 2105234.
[40] G. T. Hitz, D. W. McOwen, L. Zhang, Z. Ma, Z. Fu, Y. Wen, Y. Gong, J. Dai, T. R. Hamann, L. Hu, et al., *Mater. Today* **2019**, *22*, 50.
[41] C. Yang, L. Zhang, B. Liu, S. Xu, T. Hamann, D. McOwen, J. Dai, W. Luo, Y. Gong, E. D. Wachsman, et al., *PNAS* **2018**, *115*, 3770.
[42] F. Al-Jaljouli, R. Mücke, P. Kaghazchi, Y. J. Sohn, M. Finsterbusch, D. Fattakhova-Rohlfing, O. Guillon, *J. Energy Storage* **2023**, *68*, 107784.
[43] M. Tanemura, T. Ogawa, N. Ogita, *J. Comput. Phys.* **1983**, *51*, 191.
[44] R. Varadhan, P. Gilbert, *J. Stat. Softw.* **2010**, *32*, 1.
[45] J. T. Gostick, *Phys. Rev. E* **2017**, *96*, 023307.
[46] ITWM, Battery and Electrochemistry Simulation Tool, Available at https://www.itwm.fraunhofer.de/en/departments/sms/products-services/best-battery-electrochemistrysimulation-tool.html, **2023**, accessed: 26 June 2023.
[47] A. Latz, J. Zausch, *J. Power Sources* **2011**, *196*, 3296.
[48] A. Latz, J. Zausch, *Beilstein J. Nanobiotechnol.* **2015**, *6*, 987.
[49] H. Buschmann, J. Dölle, S. Berendts, A. Kuhn, P. Bottke, M. Wilkening, P. Heitjans, A. Senyshyn, H. Ehrenberg, A. Lotnyk, et al., *Phys. Chem. Chem. Phys.* **2011**, *13*, 19378.
[50] V. Thangadurai, D. Pinzaru, S. Narayanan, A. K. Baral, *J. Phys. Chem. Lett.* **2015**, *6*, 292.
[51] X. Han, Y. Gong, K. K. Fu, X. He, G. T. Hitz, J. Dai, A. Pearse, B. Liu, H. Wang, G. Rubloff, et al., *Nat. Mater.* **2017**, *16*, 572.
[52] R. Amin, Y.-M. Chiang, *J. Electrochem. Soc.* **2016**, *163*, A1512.
[53] R. Ruess, S. Schweidler, H. Hemmelmann, G. Conforto, A. Bielefeld, D. A. Weber, J. Sann, M. T. Elm, J. Janek, *J. Electrochem. Soc.* **2020**, *167*, 100532.
[54] T. Kato, T. Hamanaka, K. Yamamoto, T. Hirayama, F. Sagane, M. Motoyama, Y. Iriyama, *J. Power Sources* **2014**, *260*, 292.
[55] M. Weiss, R. Ruess, J. Kasnatscheew, Y. Levartovsky, N. R. Levy, P. Minnmann, L. Stolz, T. Waldmann, M. Wohlfahrt-Mehrens, D. Aurbach, et al., *Adv. Energy Mater.* **2021**, *11*, 2101126.
[56] M. Landstorfer, S. Funken, T. Jacob, *Phys. Chem. Chem. Phys.* **2011**, *13*, 12817.
[57] P. Ramadass, B. Haran, P. M. Gomadam, R. White, B. N. Popov, *J. Electrochem. Soc.* **2004**, *151*, A196.
[58] J. Molenda, A. Stokłosa, T. Bak, *Solid State Ionics* **1989**, *36*, 53.
[59] H. Xia, L. Lu, G. Ceder, *J. Power Sources* **2006**, *159*, 1422.
[60] Y. Lu, C.-Z. Zhao, H. Yuan, X.-B. Cheng, J.-Q. Huang, Q. Zhang, *Adv. Funct. Mater.* **2021**, *31*, 2009925.
[61] M. Ender, J. Joos, T. Carraro, E. Ivers-Tiffée, *J. Electrochem. Soc.* **2012**, *159*, A972.
[62] B. Tjaden, D. J. Brett, P. R. Shearing, *Int. Mater. Rev.* **2018**, *63*, 47.

[63] A. Bielefeld, D. A. Weber, J. Janek, *J. Phys. Chem. C* **2018**, *123*, 1626.
[64] I. N. David, T. Thompson, J. Wolfenstine, J. L. Allen, J. Sakamoto, *J. Am. Ceram. Soc.* **2015**, *98*, 1209.
[65] J. K. Eckhardt, T. Fuchs, S. Burkhardt, P. J. Klar, J. Janek, C. Heiliger, *ACS Appl. Mater. Interfaces* **2022**, *14*, 42757.
[66] F. Zhang, Q.-A. Huang, Z. Tang, A. Li, Q. Shao, L. Zhang, X. Li, J. Zhang, *Nano Energy* **2020**, *70*, 104545.
[67] M. Ihrig, M. Finsterbusch, C.-L. Tsai, A. M. Laptev, C.-h. Tu, M. Bram, Y. J. Sohn, R. Ye, S. Sevinc, S.-k. Lin, et al., *J. Power Sources* **2021**, *482*, 228905.
[68] E. Yi, W. Wang, J. Kieffer, R. M. Laine, *J. Power Sources* **2017**, *352*, 156.
[69] A. Sharafi, C. G. Haslam, R. D. Kerns, J. Wolfenstine, J. Sakamoto, *J. Mater. Chem. A* **2017**, *5*, 21491.
[70] M. Armand, P. Axmann, D. Bresser, M. Copley, K. Edström, C. Ekberg, D. Guyomard, B. Lestriez, P. Novák, M. Petranikova, et al., *J. Power Sources* **2020**, *479*, 228708.
[71] C. Wang, R. Yu, S. Hwang, J. Liang, X. Li, C. Zhao, Y. Sun, J. Wang, N. Holmes, R. Li, et al., *Energy Storage Mater.* **2020**, *30*, 98.
[72] J. Y. Kim, J. Kim, S. H. Kang, D. O. Shin, M. J. Lee, J. Oh, Y.-G. Lee, K. M. Kim, *ETRI J.* **2020**, *42*, 129.
[73] M. Rosen, M. Finsterbusch, O. Guillon, D. Fattakhova-Rohlfing, *J. Mater. Chem. A* **2022**, *10*, 2320.
[74] W. Xu, J. Wang, F. Ding, X. Chen, E. Nasybulin, Y. Zhang, J.-G. Zhang, *Energy Environ. Sci.* **2014**, *7*, 513.
[75] J. Akimoto, Y. Gotoh, Y. Oosawa, *J. Solid State Chem.* **1998**, *141*, 298.

Manuscript received: April 20, 2023
Revised manuscript received: June 26, 2023
Accepted manuscript online: July 11, 2023
Version of record online: July 25, 2023